Materials Science-Poland, 41(2), 2023, pp. 354-367
http://www.materialsscience.pwr.wroc.pl/
DOI: 10.2478/msp-2023-0025

Preparation and characterization of BiOCl/TiO_2/MMT composite materials

Biyang Tuo[1,2,*], Xiulong Shi[1,2], Jinwang Tian[1,2], Jianli Wang[3]

[1]College of Mining, Guizhou University, Guiyang 550025, China
[2]National & Local Joint Laboratory of Engineering for Effective Utilization of Regional Mineral Resources from Karst Areas, Guiyang 550025, China
[3]College of Materials and Advanced Manufacturing, Hunan University of Technology, Zhuzhou 412000, China

To broaden the light response range of TiO_2 and improve its photocatalytic activity, BiOCl/TiO_2/MMT composite materials (BTMC) with outstanding photocatalytic performance were prepared by the sol-gel method with montmorillonite (MMT) as the supporting material, tetrabutyl titanate as titanium source and, bismuth nitrate pentahydrate as the bismuth source. The properties of the prepared materials were characterized by X-ray diffractometer (XRD), surface and porosity analysis (BET), scanning electron microscopy–energy-dispersive X-ray spectroscopy (SEM-EDS), transmission electron microscopy (TEM), X-ray photoelectron spectrometry (XPS), and ultraviolet-visible diffuse reflection spectroscopy (UV-Vis DRS). When the Bi/Ti molar ratio was 20%, the composite material exhibited a slit mesoporous structure, and its specific surface area was 109.02 m^2/g, with optimum photocatalytic activity. TiO_2 and BiOCl formed the type-II heterojunction on the surface of MMT, which facilitates the transfer of photogenerated electrons and holes, thus enhancing the photocatalytic activity of BTMC-20. The results of this study indicated that BTMC-20 is a promising photocatalytic composite material and has better photocatalytic properties under visible light.

Keywords: *MMT, TiO_2, BiOCl, composite material, photocatalytic activity*

1. Introduction

Photocatalytic technology has some advantages such as mild reaction, low energy consumption, no secondary pollution [1], and the ability to effectively remove pollutants in bodies of water. Since Fujishima and Honda published a paper on the realization of water decomposition by UV light in 1972 [2], photocatalytic technology has been a matter of deep concerned for researchers locally and internationally and has now become an effective method for wastewater purification. The key for photocatalytic technology is the photocatalytic performance of the photocatalyst. Among various photocatalysts, titanium dioxide (TiO_2) is a promising photocatalyst that has many advantages [3, 4], including strong oxidation and excellent chemical stability properties. It has been widely used in wastewater treatment. However, the TiO_2 photocatalyst's defects, such as easy agglomeration [5], weak visible light response [6, 7], and wide band gap (about 3.2 eV) [8, 9], limit its practical applications; further research leading to a new approach to wastewater treatment that solves these problems has become urgent.

In order to improve the shortcomings of using TiO_2, researchers have explored many alternative possibilities. For example, Zhou's research group [10] found that loading TiO_2 onto clay minerals can enhance its adsorption capacity, photocatalytic activity, and dispersion. The enhancement is attributed to the abundant porosity and surface-active sites of clay minerals. Wu et al. [11] also utilized clay minerals to improve the photocatalytic performance of TiO_2, and results show that clay minerals are excellent carriers of TiO_2 and can effectively enhance its photocatalytic activity. Among different clay minerals, montmorillonite (MMT) is one of the most abundant [12] and has a unique layered structure and good chemical stability [13],

* E-mail: bytuo@gzu.edu.cn

© Biyang Tuo et al. 2023. This is an open access article distributed under the Creative Commons Attribution-NonCommercial-NoDerivatives 4.0 License. (http://creativecommons.org/licenses/by-nc-nd/4.0/)

Table 1. Chemical compositions of MMT (wt.%)

Composition	SiO_2	Al_2O_3	MgO	Na_2O	CaO	Fe_2O_3	TiO_2	F	K_2O	P_2O_5	other
MMT	51.62	12.24	3.13	9.80	2.01	1.60	0.13	0.28	0.04	18.78	0.37

which provide good conditions for improving the photocatalytic performance of TiO_2. Furthermore, it can also hinder the recombination of charge carriers by capturing photoelectrons through interlayer cations, and subsequently improve the photocatalytic activity of TiO_2 [14]. These studies have confirmed the feasibility of enhancing TiO_2's photocatalytic activity by the addition of clay minerals, and MMT is regarded as an outstanding support material for photocatalysts.

Although loading TiO_2 onto MMT can enhance the photocatalytic activity of TiO_2, TiO_2-MMT composite materials are still relatively inactive, mainly because TiO_2 can only be excited by ultraviolet light, which occupies less than 4% of the solar spectrum [10, 15]. The studies show that coupling TiO_2 with other photocatalysts to build a heterojunction structure is an effective means of solving this drawback [16]. In the field of the photocatalysts, BiOCl is expected to be one of the best options because it possesses high redox ability under visible light [17] and sufficient space between the layers of Cl atoms to decrease the recombination rate of photogenerated carriers [18]. Moreover, some researchers have demonstrated that the BiOCl/TiO_2 composite material shows enhanced photocatalytic performance under visible light. For instance, Li et al. [19] reported finding a BiOCl/TiO_2 hierarchical composite material with superior visible-light response and enhanced photostability. Choi et al. [20] found that prepared BiOCl/TiO_2 hybrid microspheres showed excellent photocatalytic activity under visible light irradiation. Composite materials with high photocatalytic performance under visible light can be obtained by loading BiOCl and TiO_2 onto MMT. To our knowledge, not much research has been done on the synergistic-enhanced mechanism between BiOCl, TiO_2, and MMT; most of the existing literature focuses on the interaction between the two materials.

On the basis of the above analysis, we reported BiOCl/TiO_2/MMT composite materials (BTMC) with type-II heterojunction via a sol-gel method combined with a roasting procedure. The mechanism of enhancing photocatalytic capacity among the three components was analyzed using a variety of characterization methods, and the effects of different Bi/Ti combinations (molar ratio) on the photocatalytic performance of the BTMC were explored.

2. Experimental details

2.1. Materials and reagents

MMT was purchased from the Chifeng Hengrun Industry and Trade Co., Ltd. (Inner Mongolia, China); its chemical composition is shown in Table 1. Tetrabutyl titanate ($C_{16}H_{36}O_4Ti$), bismuth nitrate pentahydrate ($Bi(NO_3)_3{\cdot}5H_2O$), and potassium chloride (KCl) were purchased from Shanghai Yien Chemical Technology Co., Ltd. (Shanghai, China). Anhydrous ethanol (C_2H_5OH) and glacial acetic acid (CH_3COOH) were purchased from Tianjin Fuyu Fine Chemical Co., Ltd. (Tianjin, China). Sodium hexametaphosphate ($(NaPO_3)_6$) was purchased from Tianjin Kemiou Chemical Reagent Co., Ltd. (Tianjin, China). Potassium iodide (KI), tert-butanol ($C_4H_{10}O$), and p-benzoquinone ($C_6H_4O_2$) were purchased from Shanghai Aladdin Reagent Co., Ltd. (Shanghai, China). Deionized water was used in all of the experiments.

2.2. Preparation of BTMC composite materials

First, BiOCl was prepared by the hydrolysis method: 12 mmol $Bi(NO_3)_3 \cdot 5H_2O$ and 12 mmol KCl were dissolved in 20 mL nitric acid and 40 mL deionized water, respectively (The solutions will be referred to as mixed solution A and B, respectively). Thereafter, the mixed solution A was dripped into the mixed solution B, stirred for 2 h

and stood for 2 h. The reaction solution was filtered, washed with both water and absolute ethanol three times each, and the filter cake was dried in an oven at 80°C for 24 h to obtain the BiOCl sample.

Then, BTMC composite materials were prepared using the sol-gel method [21] combined with the calcining (calcination) procedure and the preparation procedure shown in Figure 1. The details of the preparation method were as follows: 10 mL anhydrous ethanol was fully mixed with 5 mL glacial acetic acid, then 13.6 mL tetrabutyl titanate was slowly added and stirred for 30 min to form mixed solution C. A certain amount of MMT was dissolved in 50 mL deionized water to obtain the MMT suspension, and a certain amount of BiOCl was dispersed in the MMT suspension according to the molar ratio of Bi/Ti. The mixed solution C was slowly added to the MMT suspension, stirred for 3 h and aged for 24 h. The aged gel was dried in an oven at 80°C for 12 h, ground through a 200-mesh sieve, and then placed in a muffle furnace for calcining at 600°C for 2 h. The calcined samples are BTMC composite materials. The method of preparing TiO_2/MMT composite materials (TMC) is the same except that no BiOCl is added. When the Bi/Ti molar ratio is 10%, 15%, 20%, 25%, and 30%, it is denoted as BTMC-10, BTMC-15, BTMC-20, BTMC-25, and BTMC-30 in sequence.

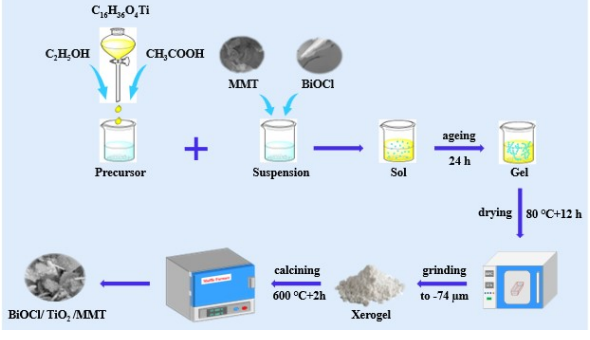


Fig. 1. The schematic illustration of the synthesis process of BTMC composite materials

2.3. Characterizations

The phase composition of the composite material was analyzed using the Bruker D8 Advance X-ray diffractometer (XRD, Germany). The composite material was irradiated by Cu Kα ($\lambda = 1.5418$ Å) at 40 kV and 40 mA at a scanning rate of 5°/min. The measurement range of $2\theta$is 10°~80°. The specific surface area and pore structure characteristics of the composite material were measured by using the Micromeritics APSP 2460 specific surface and porosity analyzer (BET, American). The surface morphology of the composite material was observed using a Zeiss Merlin compact scanning electron microscope (SEM, Germany). Microstructure of the composite was analyzed using the G2 F20 S-TWIN TMP transmission electron microscopy (TEM, American). The Thermo Scientific K-Alpha X-ray photoelectron spectrometer (XPS, American) and Al Ka monochromatized sources were used to analyze the elemental composition and elemental valence state of the composite material, respectively. A UV-3600 (UV-Vis DRS, Japan) spectrophotometer was used to analyze UV-Vis absorption spectroscopy. The wavelength ranged from 200 to 800 nm, and the measurement interval was 1 nm.

3. Results and discussion

3.1. XRD analysis

Figure 2a shows the XRD images of MMT. As can be seen from the figure, the diffraction peaks located at 22.1°, 29.2°, and 36.2° are the same as the standard card peaks of cristobalite (JCPDS No. 39-1425). At the same time, the diffraction peaks located at 6.50°, 19.9°, 26.7°, and 62.0° can also be accurately indexed to the standard XRD card of sodium montmorillonite (JCPDS No. 29-1498). The XRD results show that MMT belongs to sodium montmorillonite and the impurity is cristobalite, which is consistent with the chemical composition analysis results of MMT (shown in Table 1).

Figure 2b shows the XRD patterns of BiOCl, TiO_2, TMC, BTMC-10, BTMC-15, BTMC-20, BTMC-25, and BTMC-30. It can be seen from Figure 2a that the diffraction peaks located at 25.4°, 38.0°, 48.3°, 54.1°, 55.2°, 62.6°, and 62.9° in the TMC sample belong to the characteristic peaks of

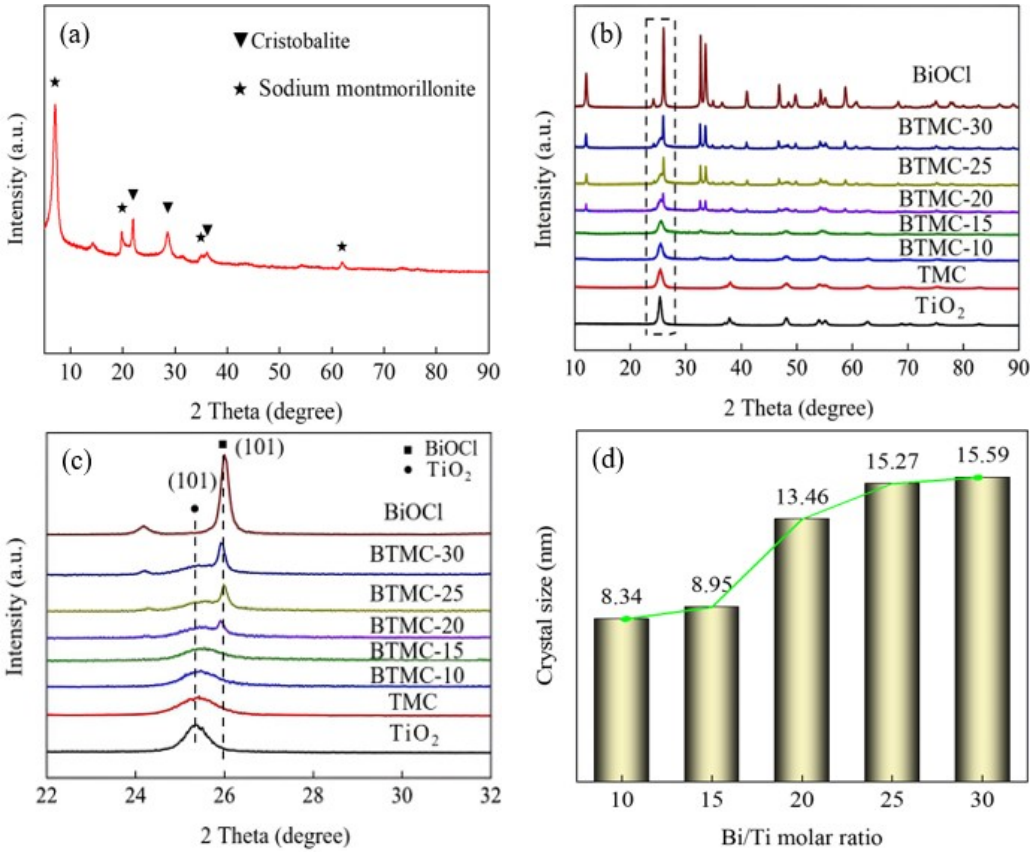


Fig. 2. The XRD patterns of samples (a–c) and the crystal size of BTMC composite materials (d)

anatase phase TiO_2 (JCPDS NO. 21-1272), indicating that TiO_2 supported on the surface of MMT exists in the form of anatase phase. The characteristic diffraction peaks of the rutile-phase TiO_2 were not observed in the TMC sample after calcining at 600° for 2 h, which indicated that MMT can restrain the conversion of anatase to rutile [22]. By comparing the diffraction peaks of TiO_2 and TMC at 25.4°, it can be found that the addition of MMT significantly reduces the diffraction peak intensity corresponding to the (101) crystal plane of TiO_2, indicating that MMT has a certain inhibition effect on the crystallization of TiO_2, thus affecting the photocatalytic activity of the composite material [23, 24].

To better observe the influence of BiOCl on the structure of BTMC, Figure 2b was locally enlarged (Figure 2c). As can be seen from Figure 2c, with the increase of BiOCl content, the intensity of the diffraction peak corresponding to the (101) crystal plane in the TiO_2 gradually weakens and the (101) crystal plane slowly moves to a low angle. This is because Ti^{4+} replaces Bi^{3+}, creating a lattice defect [25]. In order to further explore the effect of Ti^{4+} replacing Bi^{3+} on the crystal structure of BTMC, the Scherrer formula [26] (Eq. 1) was used to estimate the crystal size of BTMC, and the results are shown in Figure 2d. With the gradual increase of BiOCl content, the grain size of the material gradually increased. In addition, when the Bi/Ti molar ratio is 20%, the diffraction peak corresponding to the (101) crystal plane in BiOCl appears, indicating that the degree of combination for BiOCl and TiO_2 is optimal at this time, and increasing further BiOCl content will inhibit the growth of TiO_2 crystal, thus decreasing the photocatalytic activity of the composite materials [27, 28].

$$D = K\lambda / B\cos\theta \tag{1}$$

Where D is the grain diamter perpendicular to the

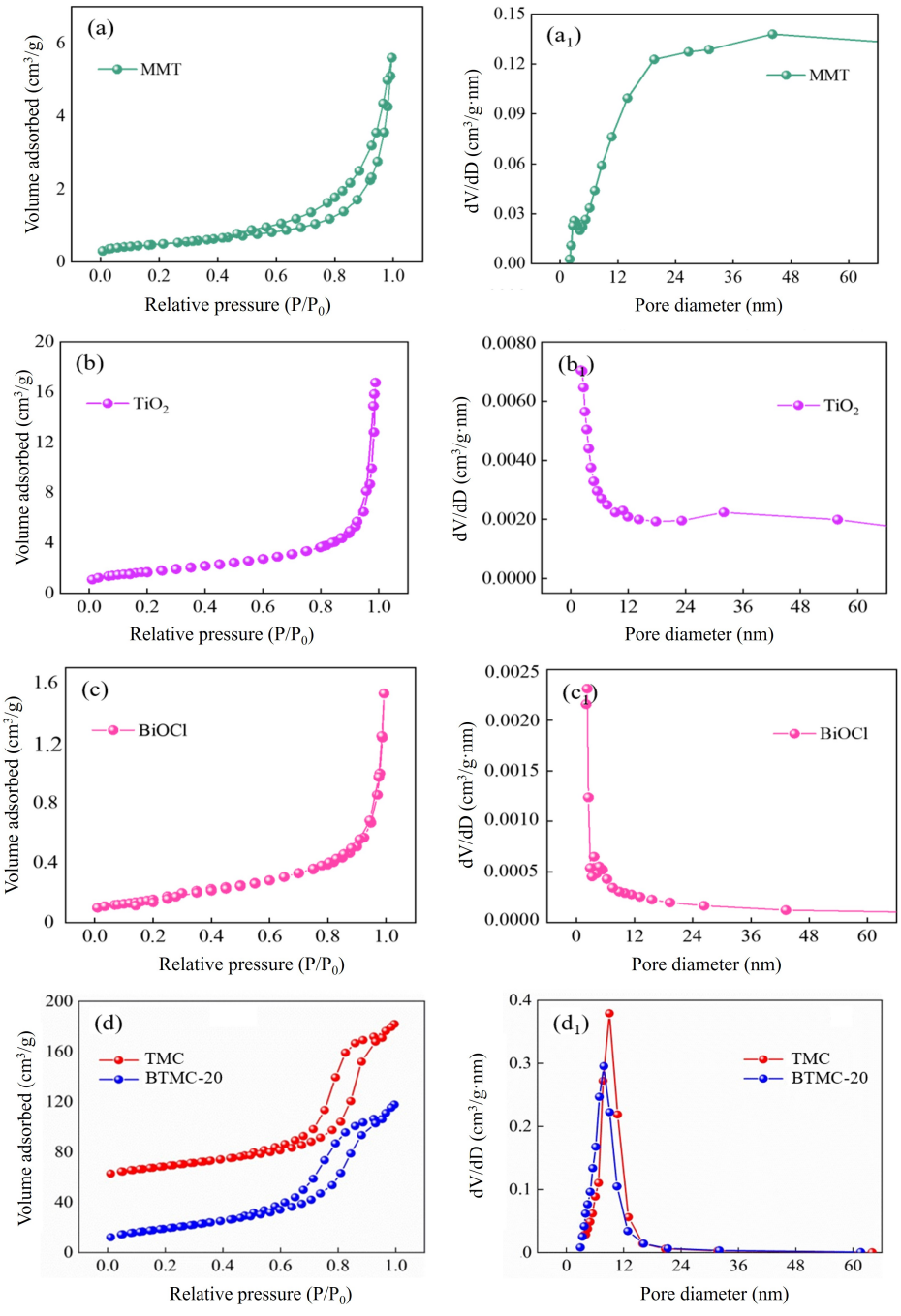


Fig. 3. The nitrogen adsorption-desorption isotherms and pore size distribution curves of five samples

crystal plane, nm. K is Scherrer's constant, which generally is 0.89. λ is the wavelength of incident X-ray, which is 0.15406 nm. B is the half-peak width of diffraction peak, and rad. θ is the degree of the Bragg diffraction angle.

3.2. BET analysis

The specific surface area and pore structure are important factors affecting the photocatalytic performance of composite material. Therefore, N_2 pore size distribution of five samples. As can be

Table 2. BET test data of materials

Materials	Specific surface area (m^2/g)	Mean aperture (nm)
MMT	39.20	19.84
TiO_2	6.09	18.43
BiOCl	0.59	14.01
TMC	97.46	11.05
BTMC-20	109.02	9.52

seen from the International Union of Pure and Applied Chemistry (IUPAC), the N_2 adsorption–desorption isotherm curve of MMT (Figure 3a) belongs to a type III isotherm with an obvious hysteresis loop, indicating that the presence of mesoporous material (2 nm~50 nm) inside the MMT. When $P/P_0<0.4$, the adsorption capacity slowly increases and presents a platform, indicating that no micropores exist in the MMT. When $0.4<P/P_0<0.9$, the adsorption volume began to rise gradually. When $P/P_0>0.9$, the adsorption volume rises sharply, indicating that MMT had multilayer adsorption and capillary condensation. The micropores and small pores were filled with a large amount of N_2, and there were more mesoporous and macroporous structures inside the MMT. The adsorption-desorption isotherm curves of TiO_2 (Figure 3b) and BiOCl (Figure 3c) also exhibited a typical type III isotherm: the characteristics of the curves are similar to MMT, but there is no obvious hysteresis loop, indicating that they are also mesoporous material and that there are many mesoporous and macroporous structures inside them. After TiO_2 is loaded onto MMT, the N_2 adsorption-desorption isotherm curve changes from type III isotherm to type IV isotherms with a more obvious hysteresis loop, indicating that there are many mesoporous structures inside TMC [29]. In Figure 3d, the N_2 adsorption-desorption isotherm curve of BTMC-20 belongs to type IV isotherms with a more obvious hysteresis loop.

Figure $3a_1$-d_1 and Table 2 show pore size distribution curves and the BET data of the materials, respectively. In Figure $3a_1$-c_1, the pore size of MMT, TiO_2, and BiOCl is mainly distributed between 2.75 nm~24 nm, which is consistent with their average pore sizes (MMT:19.84 nm; TiO_2:18.43 nm; BiOCl:14.01 nm). The pore diameter of TMC and BTMC-20 was centered at 11.05 nm and 9.52 nm (Figure $3d_1$), respectively, again showing the mesoporous structure in the composite materials. Furthermore, the pore size of the BTMC-20 was slightly reduced after adding BiOCl, which was attributed to the presence of BiOCl inhibiting the growth of TiO_2 crystals [30].

As can be seen from Table 2, the specific surface area of MMT, TiO_2, and BiOCl are 39.20 m^2/g, 6.09 m^2/g, and 0.59 m^2/g, respectively. It is not difficult to see that the specific surface area of MMT is the largest, which is consistent with its physical properties. After adding TiO_2, the specific surface area increased to 97.46 m^2/g, an increase of 58.26 m^2/g. Compared with TMC, the specific surface area of BTMC-20 (109.02 m^2/g) increased more significantly. The increase of the specific surface area is conducive to the absorption of photons by the material, thus enhancing the photocatalytic activity [31]. This shows that loading TiO_2 and BiOCl onto MMT can effectively improve the photocatalytic performance of the material.

3.3. SEM analysis

Figure 4 shows the SEM images of MMT, BiOCl, TMC, and BTMC-20. It can be seen from Figure 4a that the MMT has a clear layered structure, and its lamellar layer is stripped to a certain extent, which accords with the micromorphological characteristics of MMT [32]. As Figure 4b shows, BiOCl has an obvious two-dimensional layered structure and an accumulation of layers with layers, indicating that BiOCl nanosheets have high crystallity and a large specific surface area, which is conducive to the separation of photogenerated electron-hole pairs, thus improving the photocatalytic activity of the samples [33]. In comparison with the SEM image of MMT, the micromorphol-

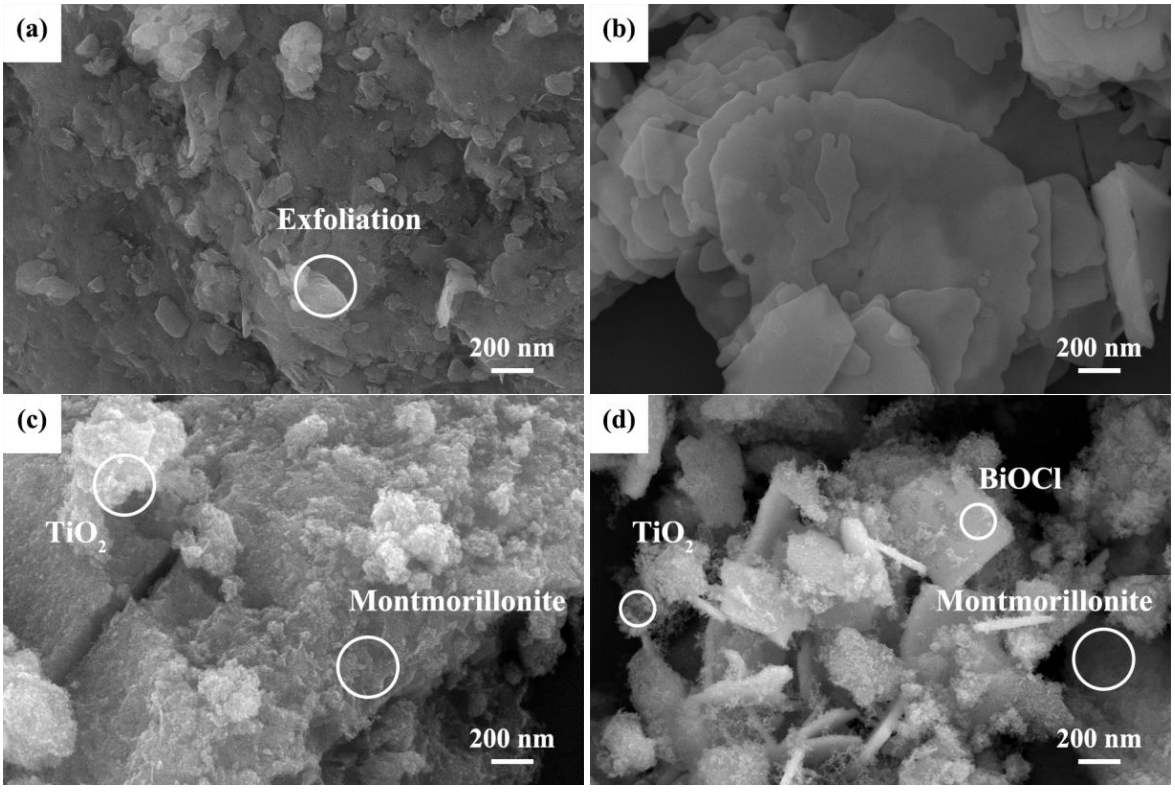


Fig. 4. The SEM images of MMT (a), BiOCl (b), TMC (c), BTMC-20 (d)

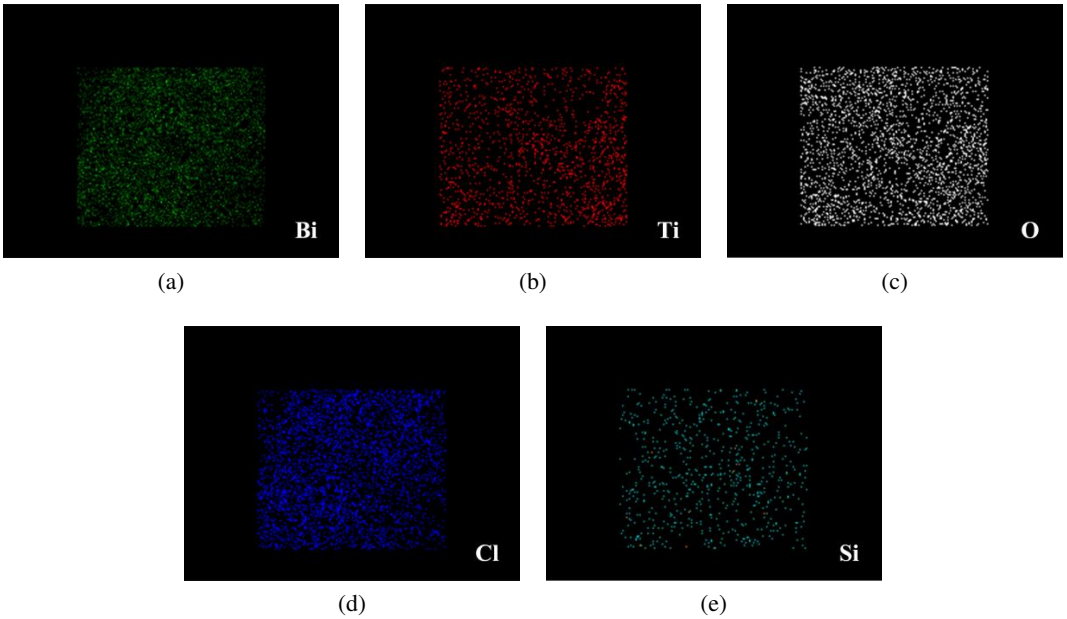


Fig. 5. The EDX mapping image of BTMC-20

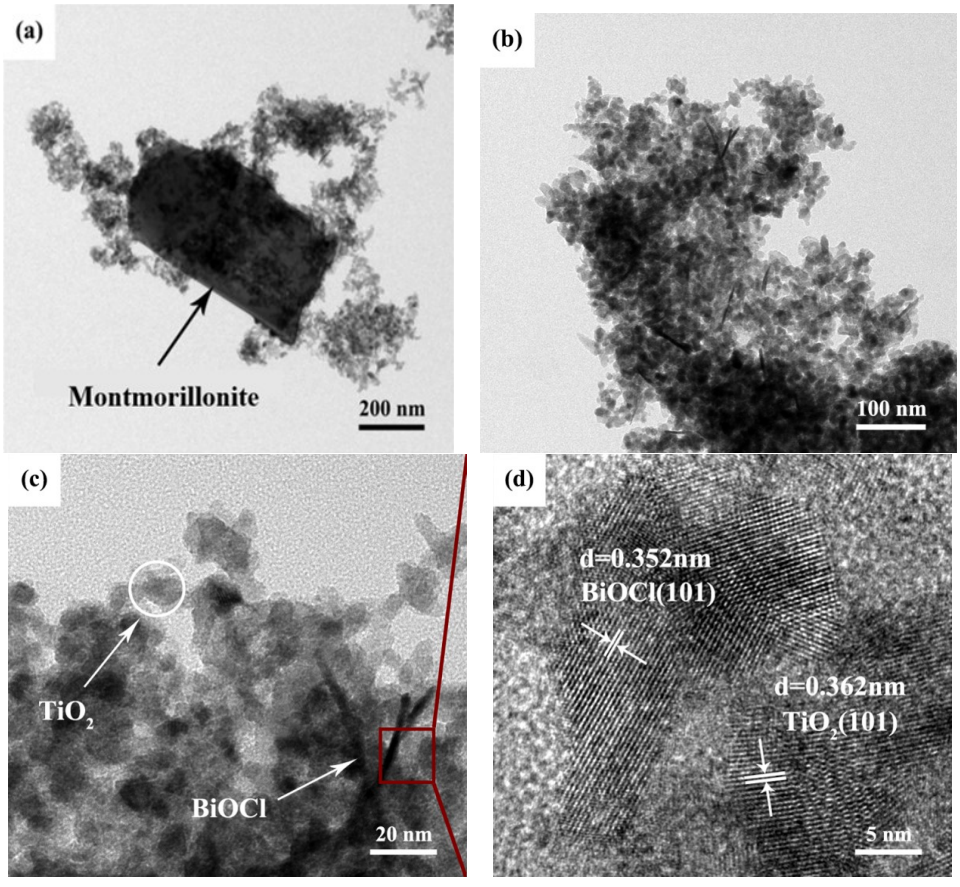


Fig. 6. The TEM images of BTMC-20

ogy of TMC was obviously changed, and a slit mesopore appeared (Figure 4c), which is consistent with the result that TMC has an H_3-type hysteresis ring. In addition, a large number of TiO_2 particles were loaded on the MMT, which destroyed its original layered structure, and this is consistent with the disappearance of MMT diffraction peaks in the XRD pattern. This is attributed to the polyhydroxy-cationic Ti^{4+} entering the middle of the MMT layer, which expands the crystal plane spacing and generates serious peeling phenomena between the interlamellars and then results in the formation of different sizes of slit mesoporous structures in the process of calcining and crystallization [34]. As can be seen from Figure 4d, a large number of BiOCl nanoparticles can be observed in the BTMC-20. TiO_2 is the shape of cotton batting, and its particle size became significantly smaller, indicating that the addition of BiOCl can inhibit the growth of TiO_2 crystal. The flocculent TiO_2 on the surface of BiOCl nanosheets is adsorbed onto the surface of MMT, which indicates that BiOCl/TiO_2 heterojunction has formed and is supported on the surface of MMT.

Figure 5 shows the EDX mapping of BTMC-20, and it was obtained by surface energy spectrum analysis of the graph interval of BTMC-20 in Figure 4d. BTMC-20 is mainly composed of Ti, O, Bi, Cl, and Si elements, indicating that BiOCl, TiO_2, and MMT coexist in BTMC, which further confirms the successful preparation of BTMC-20. Comparison of the Ti and Bi elements shows that the distribution of Ti elements is more uniform, while the distribution of Bi elements is more concentrated, indicating that the lamellar accumulation of BiOCl greatly improves the dispersion of TiO_2 particles.

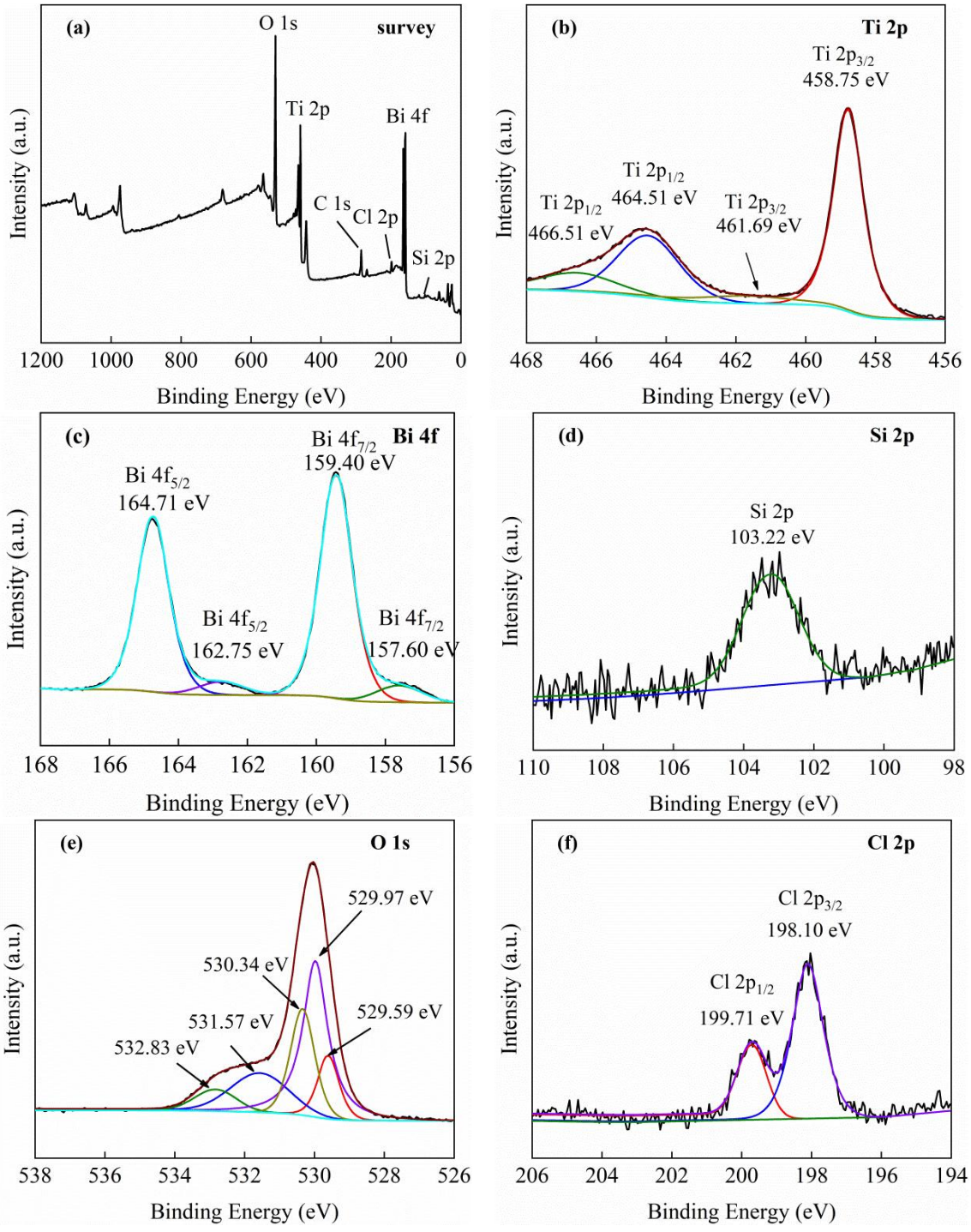


Fig. 7. (a) The XPS of BTMC-20, (b) the high-resolution Ti 2p, (c) Bi 4f, (d) Si 2p, (e) O 1s, (f) Cl 2p of sample

3.4. TEM analysis

Figure 6 shows the TEM images of BTMC-20. From Figure 6a and 6b, it can be observed that the MMT with a flake structure was supported by a large number of black linear and granular materials on its surface, indicating that BiOCl and TiO_2 have been successfully supported on the surface of

the MMT. To further determine the composition of black linear and granular materials, part of Figure 6c was enlarged to get Figure 6d. It can be observed that the lattice fringe with an interplanar spacing of 0.352 nm corresponds to the (101) crystal plane of BiOCl, and the lattice fringe with an interplanar spacing of 0.362 nm represents the TiO_2 (101) crystal plane of anatase phase [35], which demonstrates that the black linear material is BiOCl, and the granular material is anatase phase TiO_2. This also provides strong support for the successful preparation of the BTMC-20. Moreover, it can be seen from Figure 6c that TiO_2 and BiOCl are closely combined and exist in the form of accumulation and plane assembly, indicating that the heterojunction structure formed between BiOCl and TiO_2, which is conducive to the separation of photogenerated electron-hole pairs.

3.5. XPS analysis

Figure 7a shows the XPS of BTMC-20. The electron-binding energy peaks of O 1s, Ti 2p, C 1s, Cl 2p, Bi 4f, and Si 2p can be clearly observed, and correspond to O, Ti, C, Cl, Bi, and Si, respectively. This is consistent with the element composition of BTMC-20 determined in Figure 5a–e. Moreover, the peaks of other impurities were not observed in the figure, indicating that the purity of BTMC-20 is relatively high. Figure 7b–f shows the fine spectra of the Ti 2p, Bi 4f, Si 2p, O 1s, and Cl 2p, respectively. As can be seen from Figure 7b, there are two strong peaks located at 458.75 eV and 464.51 eV derived from the Ti $2p_{3/4}$ and Ti $2p_{1/2}$ orbital of TiO_2, respectively, which indicate that the Ti element exists in the form of a +4 valence state in BTMC-20 [36]. From Figure 7c, we can see that there are two strong peaks located at 159.40 eV and 164.71 eV, corresponding to the characteristic peaks of Bi $4f_{7/2}$ and Bi $4f_{5/2}$, respectively, indicating that the Bi element exists in the form of a +3 valence state in BTMC-20 [37]. The electron-binding, energy-binding peak at 103.22 eV is attributed to the typical Si-O bond (Figure 7d). In Figure 7e, the four strong peaks appear at 529.97, 530.34, 531.57, and 532.83 eV, corresponding to $[Bi_2O_2]^{2-}$, Ti-O-Ti, surface OH, and Si-O-Si bond [38], respectively. From the Cl 2p spectra (Figure 7f), it can be found that two peaks located at 198.10 eV and 199.71 eV correspond to the characteristic peaks of Cl $2p_{3/2}$ and Cl $2p_{1/2}$, respectively, indicating that the Cl element exists in the form of a −1 valence state in BTMC-20.

3.6. UV-Vis DRS analysis

Figure 8 shows the ultraviolet diffuse reflectance spectra (DRS) and band gaps of BiOCl, TiO_2, TMC, and BTMC-20. The band-edge absorption of BiOCl and TiO_2 are 364 nm and 389 nm, respectively, both of which are in the ultraviolet region, indicating that BiOCl and TiO_2 have good absorption capacity in the ultraviolet region, which is consistent with previous reports [39, 40]. Compared with pure TiO_2, the band-edge absorption of TMC (394 nm) showed a weak redshift, indicating that the addition of MMT can improve the light absorption capacity of the composite material. After compounding with BiOCl, the band-edge absorption is redshifted to 417 nm (BTMC-20). Compared with BiOCl, TiO_2, and TMC, the light absorption range of BTMC-20 extends to the visible light region, which indicates that the light-response range of BTMC-20 was broadened and its visible light absorption capacity was enhanced, thus enhancing the photocatalytic activity of BTMC-20.

The band gaps of BiOCl, TiO_2, TMC, and BTMC-20 are calculated according to formula (Eq. 2), and the results are shown in Figure 8b.

$$(\alpha h\nu)^{1/n} = A(h\nu - E_g) \tag{2}$$

Where α is the absorption coefficient, $h\nu$ is the binding energy, eV. A is absorbance (abs), E_g is the band gap, eV. n is the power index, which is determined by the type of electronic transition (for direct bandgap materials, n = 1/2, and for indirect bandgap materials, n = 2). Here, the value of n is taken as 2 [41]. The band gaps of BiOCl, TiO_2, TMC, and BTMC-20 are 3.27 eV, 3.06 eV, 2.89 eV, and 2.61 eV, respectively. The band gap of TMC is lower than that of TiO_2, which indicates that the addition of MMT can improve the photocatalytic activity of TMC. Among them, BTMC-20 has the smallest band gap (2.61 eV), which indicates that it

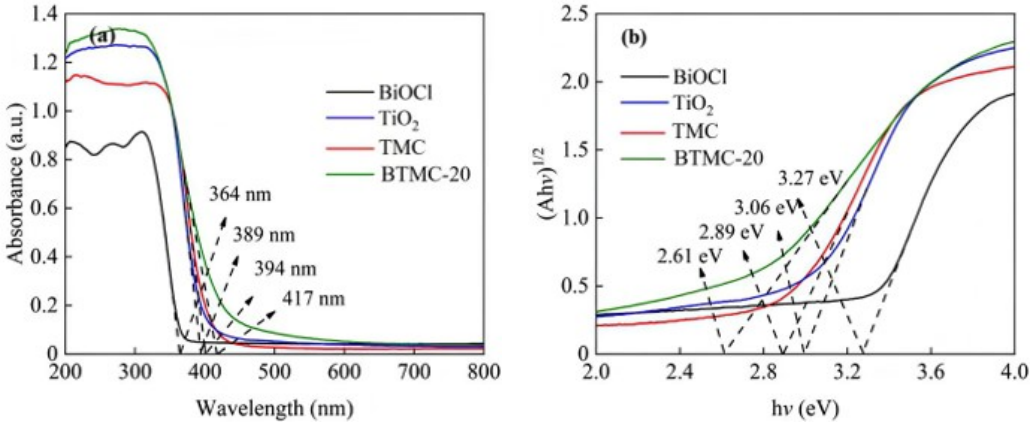


Fig. 8. The UV–vis spectra (a) and band gaps of BiOCl, TiO_2, TMC, and BTMC-20 (b)

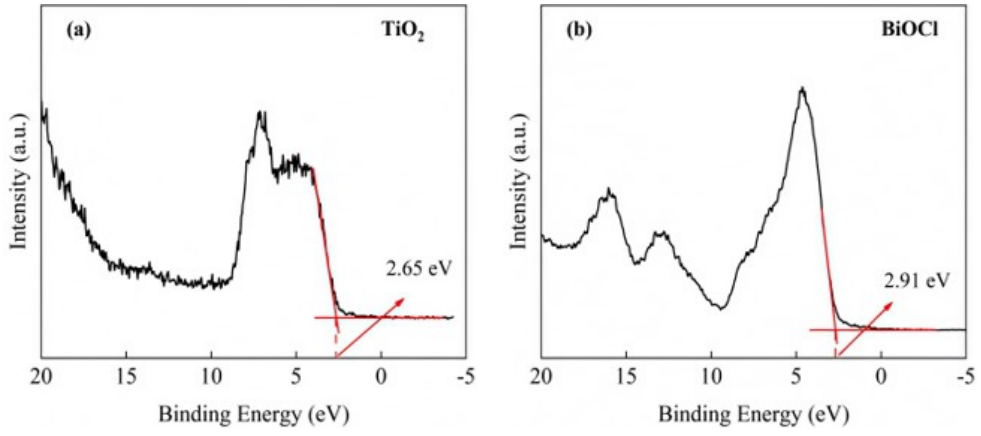


Fig. 9. The valence-band XPS spectrum of TiO_2 (a) and BiOCl (b)

has higher photocatalytic activity and stronger light response. The main reason is that a heterojunction (type II) can be formed between BiOCl and TiO_2 because of their different conductance and valence band potential [42]. In the meantime, in the process of calcining–crystallization, BiOCl and TiO_2 replace Bi (III) and Ti (IV) elements with each other to form impurity levels, thus reducing the band gap [43].

It can be seen from Figure 9a and 9b that the valence band potential values (E_{VB}) of TiO_2 and BiOCl are 2.65 eV and 2.91 eV, respectively. The band gaps of TiO_2 and BiOCl are 3.06 and 3.27, respectively, as calculated by the band gap of DRS (Figure 8b). So, the conduction band potential values (E_{CB}) of TiO_2 and BiOCl can be calculated as -0.41 eV and -0.36 eV according to the formula $E_{VB} = E_{CB} + E_g$ [44]. The above analysis demonstrated that BiOCl combines with TiO_2 on the MMT to form a type II heterojunction, thus accelerating the transfer of photogenerated electrons and holes [45].

4. Conclusions

1. The XRD analysis results show that MMT is sodium montmorillonte, and the main impurity is cristobalite. TiO_2 exists in BTMC as anatase crystal phase. The addition of MMT can inhibit the conversion of anatase to rutile, and excess BiOCl will inhibit the growth of TiO_2 crystal. Moreover, with the increase of BiOCl content, the crystal size of BTMC gradually increases.

2. The BET analysis results show that the adsorption–desorption curves of MMT, TiO_2, and BiOCl are all type III isotherm, and their mean apertures are 19.84 nm, 18.43 nm, and 14.01 nm, respectively. TMC and BTMC-20 belong to type IV isotherm, and their mean apertures are 11.05 nm and 9.52 nm, respectively. Loading TiO_2 and BiOCl onto MMT can increase the specific surface area of the materials, thus enhancing the photocatalytic activity.
3. The SEM and TEM analysis results show that both MMT and BiOCl have layered structures, and TMC has a narrow mesoporous structure. The (101) crystal plane spacing of BiOCl and TiO_2 was 0.352 nm and 0.362 nm, respectively.
4. The XPS and UV-Vis DRS analysis results show that Ti, Bi, and Cl are present in BTMC-20 as +4, +3, and −1 valence states, respectively. The formation of BiOCl/TiO_2 heterojunction reduced the band gap from 2.89 eV to 2.61 eV, thus broadening the light response range and improving the photocatalytic activity. This study provides a new way to enhance the photocatalytic activity of TiO_2, and BTMC composite materials have promising application prospects in the photodegradation of pollutants in water, providing a new approach for environmental governing.

Acknowledgements

This work was supported by the National Natural Science Foundation of China (Grant No. 51464007), the Science and Technology Support Plan of Guizhou Province (Grant No. [2021]482), and the General Projects of Hunan Provincial Education Department (Grant No. 22C0316).

References

[1] Deng F, Shi H, Guo Y, Luo X, Zhou J. Engineering paths of sustainable and green photocatalytic degradation technology for pharmaceuticals and organic contaminants of emerging concern. *Curr Opin Green Sustain Chem*. 2021;29:100465. DOI:10.1016/j.cogsc.2021.100465.

[2] Fujishima A, Honda K. Electrochemical photolysis of water at a semiconductor electrode. *Nature*. 1972;238:37–38. DOI:10.1038/238037a0.

[3] Colomer MT, Duarte KJ, Ortiz AL, Mercado DF, Ballesteros-Rueda LM. Influence of Pr^{3+} doping on the synthesis of colloidal sols and nanoparticulate TiO_2 xerogels and their photocatalytic activity. *Mater Charact*. 2021;182:111536. DOI:10.1016/j.matchar.2021.111536.

[4] Nakata K, Fujishima A. TiO_2 photocatalysis: design and applications. *J Photoch Photobio C*. 2012;13:169–189. DOI:10.1016/j.jphotochemrev.2012.06.001.

[5] Gilja V, Katancic Z, Krehula LK, Mandic V, Hrnjak-Murgic Z. Efficiency of TiO_2 catalyst supported by modified waste fly ash during photodegradation of RR45 dye. *Sci Eng Compos Mater*. 2019;26. DOI:10.1515/secm.2019.0017.

[6] Li JN, Wu F, Shi JY, Ma L, Yan XB, Yang N, Ding BF, Zheng SK. First-principles calculation of Cr/S co-doped rutile TiO_2. *Mater Sci-Pol*. 2020;38:253–262. DOI:10.2478/msp.2020.0042.

[7] Mathur AS, Kumar P, Singh BP. Comparative study of absorption band edge tailoring by cationic and anionic doping in TiO_2. *Mater Sci-Pol*. 2018;36:435–438. DOI:10.2478/msp.2018.0060.

[8] Yousef A. Fabrication of heterojunction $MnTiO_3$-TiO_2-decorated carbon nanofibers via electrospinning as an effective multifunctional photocatalyst. *Mater Sci-Pol*. 2022;40:289–305. DOI:10.2478/msp.2022.0028.

[9] Zou YL, Huang XS, Yu T, Tong XQ, Li Y, Lian XX, Xie Y, Huang JM, He W, Li WX. Cu-doped TiO_2 brookite photocatalyst with enhanced visible light photocatalytic activity. *Mater Sci-Pol*. 2020;38:644–653. DOI:10.2478/msp.2020.0074.

[10] Zhou P, Shen Y, Zhao S, Li G, Cui B, Wei D, et al. Synthesis of clinoptilolite-supported BiOCl/TiO_2 heterojunction nanocomposites with highly-enhanced photocatalytic activity for the complete degradation of xanthates under visible light. *Chem Eng J*. 2021;407:126697. DOI:10.1016/j.cej.2020.126697.

[11] Wu A, Wang D, Wei C, Zhang X, Liu Z, Feng P, et al. A comparative photocatalytic study of TiO_2 loaded on three natural clays with different morphologies. *Appl Clay Sci*. 2019;183:105352. DOI:10.1016/j.clay.2019.105352.

[12] Zhao J, Huang B, Gao W, Zheng L, Song P, He M. Periodic DFT study on heavy metals Cu(II) and Pb(II) atoms adsorption on Na-montmorillonite (010) edge surface. *Solid State Commun*. 2023;366:115171. DOI:10.1016/j.ssc.2023.115171.

[13] Uddin MK. A review on the adsorption of heavy metals by clay minerals, with special focus on the past decade. *Chem Eng J*. 2017;308:438–462. DOI:10.1016/j.cej.2016.09.029.

[14] Mishra A, Mehta A, Sharma M, Basu S. Impact of Ag nanoparticles on photomineralization of chlorobenzene by TiO_2/bentonite nanocomposite. *J Environ Chem Eng*. 2017;5:644–651. DOI:10.1016/j.jece.2016.12.042.

[15] Zhang Y, Park M, Kim HY, Ding B, Park S. In-situ synthesis of nanofibers with various ratios of

$BiOCl_x/BiOBr_y/BiOI_z$ for effective trichloroethylene photocatalytic degradation. *Appl Surf Sci*. 2016;384:192–199. DOI:10.1016/j.apsusc.2016.05.039.

[16] Zhang D, Tang Y, Qiu X, Yin J, Su C, Pu X. Use of synergistic effects of the co-catalyst, p-n heterojunction, and porous structure for improvement of visible-light photocatalytic H_2 evolution in porous $Ni_2O_3/Mn_{0.2}Cd_{0.8}S/Cu_3P@Cu_2S$. *J Alloy Compd*. 2020;845:155569. DOI:10.1016/j.jallcom.2020.155569.

[17] Li H, Li J, Ai Z, Jia F, Zhang L. Oxygen vacancy-mediated photocatalysis of BiOCl: reactivity, selectivity, and perspectives. *Angew Chem Int Edit*. 2018;57:122–138. DOI:10.1002/anie.2017.05628.

[18] Wang X, Ni Q, Zeng D, Liao G, Wen Y, Shan B, et al. $BiOCl/TiO_2$ heterojunction network with high energy facet exposed for highly efficient photocatalytic degradation of benzene. *Appl Surf Sci*. 2017;396:590–598. DOI:10.1016/j.apsusc.2016.10.201.

[19] Li W, Tian Y, Li H, Zhao C, Zhang B, Zhang H, et al. Novel $BiOCl/TiO_2$ hierarchical composites: synthesis, characterization and application on photocatalysis. *Appl Catal A-Gen*. 2016;516:81–89. DOI:10.1016/j.apcata.2016.02.006.

[20] Choi YI, Jeon KH, Kim HS, Lee JH, Park SJ, Roh JE, et al. TiO_2/BiOX (X=Cl, Br, I) hybrid microspheres for artificial waste water and real sample treatment under visible light irradiation. *Sep Purif Technol*. 2016;160:28–42. DOI:10.1016/j.seppur.2016.01.009.

[21] Dulian P, Zajic J, Zukowski W. Effect of titanium source and sol-gel TiO_2 thin film formation parameters on its morphology and photocatalytic activity. *Mater Sci-Pol.* 2020;38:424–433. DOI:10.2478/msp-2020-0056.

[22] Tian JW, Tuo BY, Wang JL, Tang Y, Nie GH, Yang Y. Preparation of different crystal types TiO_2 materials and its photodegradation performance in Congo Red wastewater. *Phase Transit*. 2022;95:707–725. DOI:10.1080/01411594.2022.2107927.

[23] Gordon TR, Cargnello M, Paik T, Mangolini F, Weber RT, Fornasiero P, et al. Nonaqueous synthesis of TiO_2 nanocrystals using TiF4 to engineer morphology, oxygen vacancy concentration, and photocatalytic activity. *J Am Chem Soc*. 2012;134:6751–6761. DOI: 10.1021/ja300823a.

[24] Gu CJ, Peng TJ, Sun HJ, Lv X, Luo LM. Assembled structure and characterization of TiO_2/Montmorillonite nanocomposites. *J Synth Cryst*. 2012;41(3):771–778. DOI:10.16553/j.cnki.issn1000-985x.2012.03.019.(in Chinese)

[25] Luo Z, Wang H, Ma Y, Zhang G, Yan D, Bai X, et al. High ionic conductivity of Lu_2O_3-TiO_2 co-doped Bi_2O_3 ceramics. *Mater Res Express*. 2021;8:25001. DOI: 10.1088/2053-1591/abe014.

[26] Kalaiarasi S, Jose M. Dielectric functionalities of anatase phase titanium dioxide nanocrystals synthesized using water-soluble complexes. *Applied Physics A*. 2017;123:512. DOI: 10.1007/s00339-017-1121-0.

[27] Shinde DS, Bhange PD, Jha RK, Bhange DS. TiO_2 nanoparticles decorated on BiOCl flakes with enhanced visible light photocatalytic activity. *Chemistryselect*. 2020;5:2618–2626. DOI:10.1002/slct.201904656.

[28] Tian JW, Tuo BY, Wang JL, Tang Y, Nie GH, Yang Y, et al. Photocatalytic degradation of simulated Congo red wastewater by $BiOCl/TiO_2$/Montmorillonite composites. *Conserv Utiliz Mineral Resources.* 2022; 42(04):68–75. DOI: 10.13779/j.cnki.issn1001-0076.2022.04.008.(in Chinese)

[29] Manga KK, Zhou Y, Yan Y, Loh KP. Multilayer hybrid films consisting of alternating graphene and titania nanosheets with ultrafast electron transfer and photoconversion properties. *Adv Funct Mater*. 2009;19:3638–3643. DOI: 10.1002/adfm.200900891.

[30] Yu H, Huang B, Wang H, Yuan X, Jiang L, Wu Z, et al. Facile construction of novel direct solid-state Z-scheme AgI/BiOBr photocatalysts for highly effective removal of ciprofloxacin under visible light exposure: Mineralization efficiency and mechanisms. *J Colloid Interf Sci*. 2018;522:82–94. DOI:10.1016/j.jcis.2018.03.056.

[31] Liu J, Zhang GK. Recent advances in synthesis and applications of clay-based photocatalysts: a review. Phys Chem Chem Phys. 2014;16:8178–192. DOI: 10.1039/c3cp54146k.

[32] Yang G, Zhao H, Liu Y, Li Z, Gao F, Zhang Q, et al. Slow release fertilizers based on polyphosphate/montmorillonite nanocomposites for improving crop yield. *Arab J Chem*. 2023;16:104871. DOI:10.1016/j.arabjc.2023.104871.

[33] Yu Y, Yang Z, Shang Z, Wang X. One-step solution combustion synthesis of Bi/BiOCl nanosheets: Reaction mechanism and photocatalytic RhB degradation. *J Phys Chem Solids*. 2023;174:111172. DOI:10.1016/j.jpcs.2022.111172.

[34] An Y, Ma B, Li X, Chen Y, Wang C, Wang B, et al. A review on the roasting-assisted leaching and recovery of V from vanadium slag. *Process Saf Environ*. 2023;173:263–276. DOI:10.1016/j.psep.2023.03.013.

[35] Liu X, Duan X, Bao T, Hao D, Chen Z, Wei W, et al. High-performance photocatalytic decomposition of PFOA by $BiOX/TiO_2$ heterojunctions: Self-induced inner electric fields and band alignment. *J Hazard Mater*. 2022;430:128195. DOI:10.1016/j.jhazmat.2021.128195.

[36] Luo C, Zhao J, Li Y, Zhao W, Zeng Y, Wang C. Photocatalytic CO_2 reduction over $SrTiO_3$: correlation between surface structure and activity. *Appl Surf Sci*. 2018;447:627–635. DOI:10.1016/j.apsusc.2018.04.049.

[37] Duo FF, Wang YW, Fan CM, Mao XM, Zhang XC, Wang YF, et al. Low temperature one-step synthesis of rutile TiO_2/BiOCl composites with enhanced photocatalytic activity. *Mater Charact*. 2015;99:8–16. DOI:10.1016/j.matchar.2014.11.002.

[38] Zhang G, Sun Z, Hu X, Song A, Zheng S. Synthesis of $BiOCl/TiO_2$-zeolite composite with enhanced visible light photoactivity. *J Taiwan Inst Chem E*. 2017;81:435–444. DOI:10.1016/j.jtice.2017.09.030.

[39] Jia X, Hu C, Cao J, Cao D, Lin H, Chen S. Using wide-band-gap BiOCl to greatly enhance the photocarriers separation of AgI via in-situ Ag bridge: Interfacial electron transfer route, density functional theory calculation and mechanism study. *Appl Surf Sci*. 2022;574:151671. DOI:10.1016/j.apsusc.2021.151671.

[40] Mohammad A, Khan ME, Cho MH, Yoon T. Fabrication of binary SnO_2/TiO_2 nanocomposites under a sonication-assisted approach: tuning of band-gap and water depollution applications under visible light irradiation. *Ceram Int*. 2021;47:15073–15081. DOI:10.1016/j.ceramint.2021.02.065.

[41] Maimaitizi H, Abulizi A, Kadeer K, Talifu D, Tursun Y. In situ synthesis of Pt and N co-doped hollow hierarchical BiOCl microsphere as an efficient photocatalyst for organic pollutant degradation and photocatalytic CO_2 reduction. *Appl Surf Sci*. 2020;502:144083. DOI:10.1016/j.apsusc.2019.144083.

[42] Low J, Yu J, Jaroniec M, Wageh S, Al-Ghamdi AA. Heterojunction photocatalysts. *Adv Mater*. 2017;29: 1601694. DOI:10.1002/adma.201601694.

[43] Jiang GH, Wang RJ, Wang XH, Xi XG, Hu RB, Zhou Y, et al. Novel highly active visible-light-induced photocatalysts based on BiOBr with Ti doping and Ag decorating. *ACS Appl Mater Inter*. 2012;4:4440–4444. DOI:10.1021/am301177k.

[44] Wang S, Li D, Sun C, Yang S, Guan Y, He H. Synthesis and characterization of g-C_3N_4/Ag_3VO_4 composites with significantly enhanced visible-light photocatalytic activity for triphenylmethane dye degradation. *Appl Catal B-Environ*. 2014;144:885–892. DOI:10.1016/j.apcatb.2013.08.008.

[45] Ao M, Liu K, Tang X, Li Z, Peng Q, Huang J. $BiOCl/TiO_2$/diatomite composites with enhanced visible-light photocatalytic activity for the degradation of rhodamine B. *Beilstein J Nanotech*. 2019;10:1412–1422. DOI:10.3762/bjnano.10.139.

Received 2023-07-01
Accepted 2023-09-22